Electronic Supplementary Material (ESI) for ChemComm.

Electronic Supplementary Information

Reversible Dinitrogen Binding to [Cp'Fe(NHC)] Associated with an N_2-induced Spin State Change

Matthias Reiners, Dirk Baabe, Marc-Kevin Zaretzke, Matthias Freytag, and Marc D. Walter

Institut für Anorganische und Analytische Chemie, Technische Universität Braunschweig, Hagenring 30, 38106 Braunschweig, Germany

Table of content

1. Experimental details

General considerations. All synthetic and spectroscopic manipulations were carried out under an atmosphere of purified dinitrogen or argon, either in a Schlenk apparatus or in a glovebox. Solvents were dried and deoxygenated either by distillation under a nitrogen or argon atmosphere from sodium benzophenone ketyl (THF, pentane, diethyl ether, hexane) or by an MBraun GmbH solvent purification system (all other solvents). Elemental analyses were performed by combustion and gas chromatographic analysis with an elementar varioMICRO or elementar varioMICRO CUBE instrument. [Cp'FeI(I*i*Pr$_2$Me$_2$)] (**2**) and KC_8 were prepared according to literature procedures.[1, 2]

Synthesis of [Cp'Fe(I*i*Pr$_2$Me$_2$)] (3). *The reaction and work-up procedure were carried out under an atmosphere of purified argon.* To a stirred suspension of KC_8 (113 mg, 0.84 mmol, 1 eq.) in THF (10 mL) a solution of [Cp'Fe(I*i*PrMe$_2$)I] (**2**; 500 mg, 0.84 mmol, 1 eq.) in THF (15mL) was added at ambient temperature. The suspension immediately changed colour from light brown to an intense green. After stirring for 0.5 h the solvent was removed under dynamic vacuum and the green residue was extracted with hexane (4x 10 mL) and filtered. The solvent was removed under dynamic vacuum, the yellow-green solid was dissolved in a minimum amount of Et_2O (1-2 mL) and stored for crystallization at -30°C to yield bright green blocks. Yield: 64% (255 mg, 0.54 mmol). M.p.: 162°C (dec.). Elemental analysis calc. (%) for $C_{28}H_{49}FeN_2$: C 71.62, H 10.52, N 5.97; found: C 70.54, H 9.95, N 5.98. No mass spectra could be obtained because of the very high reactivity of complex **3**. ^{1}H NMR (300 MHz, thf-d_8, 297 K): δ = 41.15 (br.s, 6H, $\nu_{½}$ = 80 Hz, C*H*$_3$ (NHC-backbone), 9.86 (br.s, 12H, $\nu_{½}$ = 260 Hz, CH(C*H*$_3$)$_2$), –0.81 (s, 9H, $\nu_{½}$ = 140 Hz, *t*Bu-*H*), –6.60 (s, 18H, $\nu_{½}$ = 140 Hz, *t*Bu-*H*), -109.23 (br s, 2H, $\nu_{½}$ = 1200 Hz, C*H*(CH$_3$)$_2$ or Cp-C*H*) ppm. One resonance corresponding either to C*H*(CH$_3$)$_2$ or Cp-C*H* could not be observed probably attributed to severe line broadening.

Synthesis of [Cp'Fe(I*i*Pr$_2$Me$_2$)(η^1-N$_2$)] (4). *The reaction was carried out under an atmosphere of purified dinitrogen.* In a Kontes flask solution of [Cp'Fe(I*i*PrMe$_2$)I] ((**2**; 330 mg, 0.55 mmol, 1 eq.) in THF (10 mL) was added to a frozen (liquid N_2!) suspension of KC_8 (75 mg, 0.55 mmol, 1 eq.) and THF (10 mL) and the bomb vessel was closed (N_2 (1 atm, 77 K). The frozen reaction mixture was removed from the liquid N_2 cooling bath and allowed to warm to room temperature. On melting the reaction mixture changed colour from light brown to red-brown. After stirring for 0.5 h the overpressure was carefully released to the Schlenk line and the solvent was removed in oil pump vacuum. The green-brown residue was extracted with hexane (4x 10 mL) and filtered. After removing the solvent in oil pump vacuum the yellow-green solid was dissolved in a minimum amount of Et_2O (1-2 mL) and stored for crystallization at -30°C to give olive-green blocks. Yield: 60% (164 mg, 0.33 mmol). M.p.: 73°C (dec.). IR (Nujol): 1979 cm^{-1} (N_2). Elemental analysis calc. (%) for $C_{28}H_{49}FeN_4$: C 67.59, H 9.93, N 11.26; found: C 68.14, H 10.316, N 9.97. No mass spectra could be recorded because of the very high reactivity of complex **4**.

2. ^{1}H NMR spectroscopic study

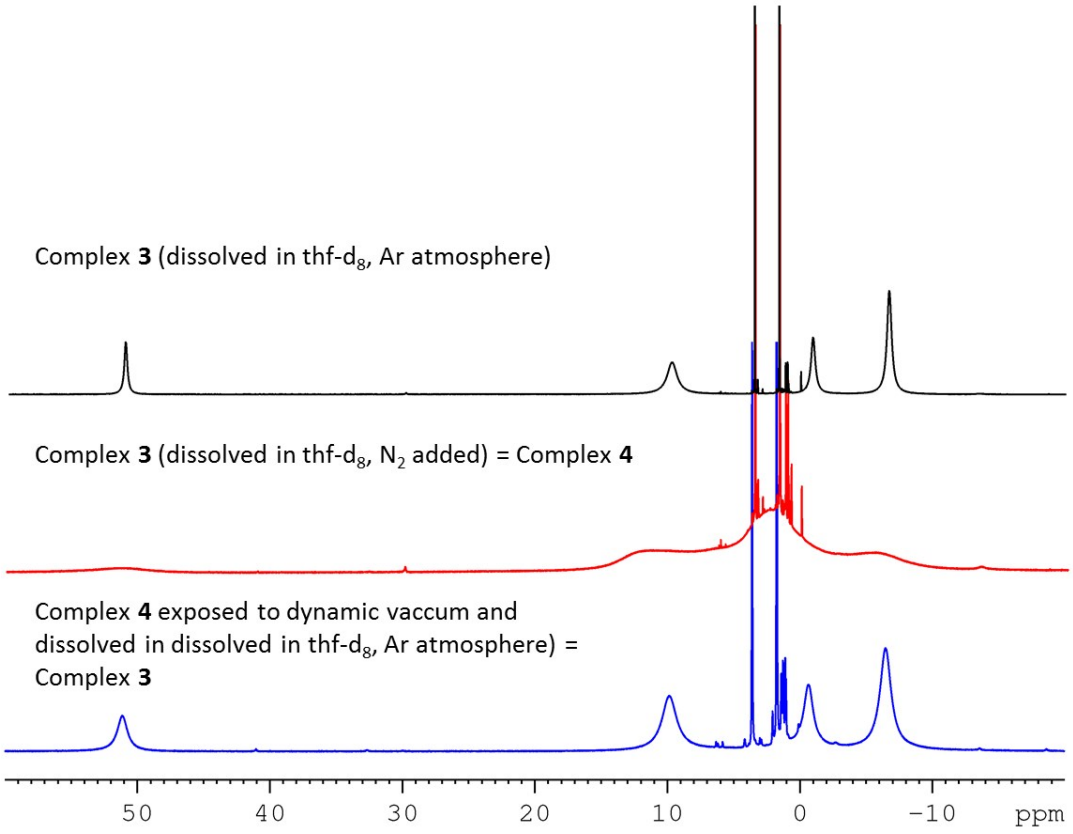

Figure S1. ^{1}H NMR spectrum recorded at 298 K in thf-d_8. (a) Complex **3** dissolved under Ar. (b) N_2 added to complex **3** in thf-d_8. (Spectrum is identical to those recorded in complex **4** under an N_2 atmosphere). (c) Solvent was removed under dynamic vacuum and the residue was redissolved in thf-d_8 under an N_2 atmosphere.

3. Crystallographic data

X-ray diffraction studies. Data were recorded at 100(2) K on Oxford Diffraction diffractometers using monochromated Mo Kα or mirror-focussed Cu Kα radiation. Absorption corrections were applied on the basis of multi-scans. The structures were refined anisotropically on F^2 using the SHELXL-97 program.[3, 4] Crystallographic data were deposited with the Cambridge Crystallographic Data Centre as supplementary publications no. CCDC-1534480-1534481. Copies of the data can be obtained free of charge from www.ccdc.cam.ac.uk/data_request/cif.

4. Solid-state magnetic susceptibility studies for 3 and 4

General considerations. Solid-state magnetic susceptibility studies were performed in quartz tubes as previously described[5] and the data were collected on a Cryogenic Ltd. closed-cycle SQUID magnetometer between T = 2.6 and 300 K with an external applied magnetic field of H_{ext} = 1 kOe. The diamagnetic background signal of the empty sample holder was experimentally determined and subtracted from the raw magnetization data. The experimental data were also corrected for the overall diamagnetism of the investigated molecules using tabulated Pascal constants.[6] Supplementary measurements at temperatures between 2.6 and 10.7 K for complex **3** and at T = 2.6 K for complex **4** with externally applied magnetic fields between 0.5 and 70 kOe were performed to determine the validity of the Curie-law approximation (Figure S3). To find experimental evidence for a possible SMM behaviour of complex **3,** time-dependent magnetization measurements at low temperatures were performed. These measurements were executed after a 70 kOe field-cooling sequence (from T = 30 K down to T = 1.587 and 2.593 K) in zero applied magnetic fields (Figure S4). Finally, we investigated the (partial) N_2 release for complex **4** at elevated temperatures and the subsequent binding of the released N_2 at lower temperatures (Figures S5 and S6). A detailed description of the heating and cooling sequences is given in the figure caption (*vide infra*).

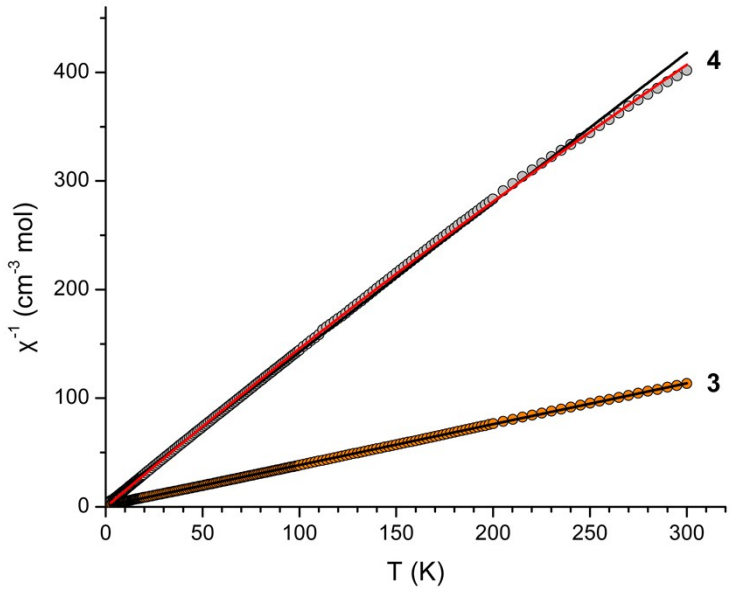

Figure S2. Inverse magnetic susceptibility (χ^{-1}) vs. T plots for **3** (orange) and **4** (grey) recorded at temperatures between T = 2.6 and 300 K with an applied magnetic field of H_{ext} = 1 kOe. Symbols: experimental data; black lines: adaptation of the Curie-Weiss law; for complex **3**: C = 2.656(2) cm^3 K mol^{-1}, Θ= -2.19(8) K, μ_{eff} = 4.61 μ_B; for complex **4**: C = 0.726(2) cm^3 K mol^{-1}, Θ= -3.3(3) K, μ_{eff} = 2.41 μ_B; red line: fit on the basis of an extended Curie-Weiss law including a temperature independent paramagnetic (TIP) contribution; for complex **4**: C = 0.660(2) cm^3 K mol^{-1}, Θ= -0.24(15) K, TIP = 2.55(8) x 10^{-4} cm^3 K mol^{-1}, μ_{eff} = 2.30 μ_B.

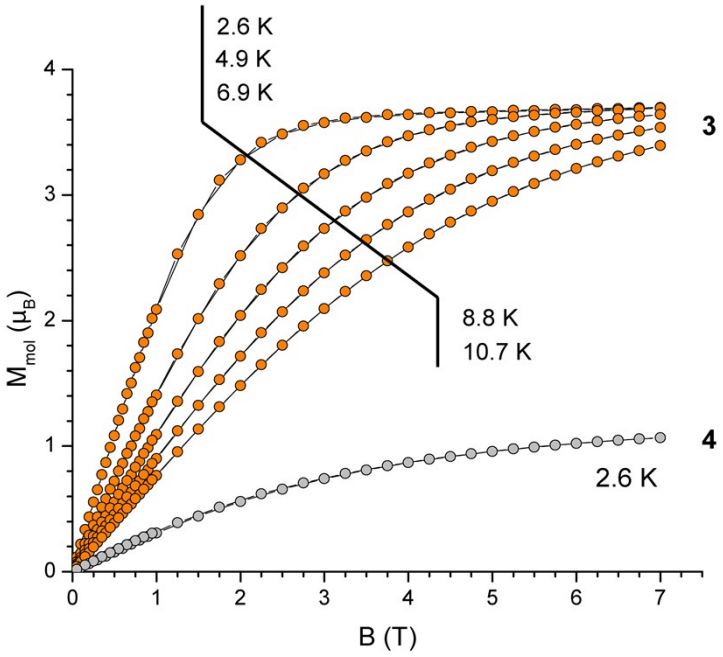

Figure S3. Molar magnetization (M_{mol}) vs. magnetic field (B) plot for **3** (orange) and **4** (grey).

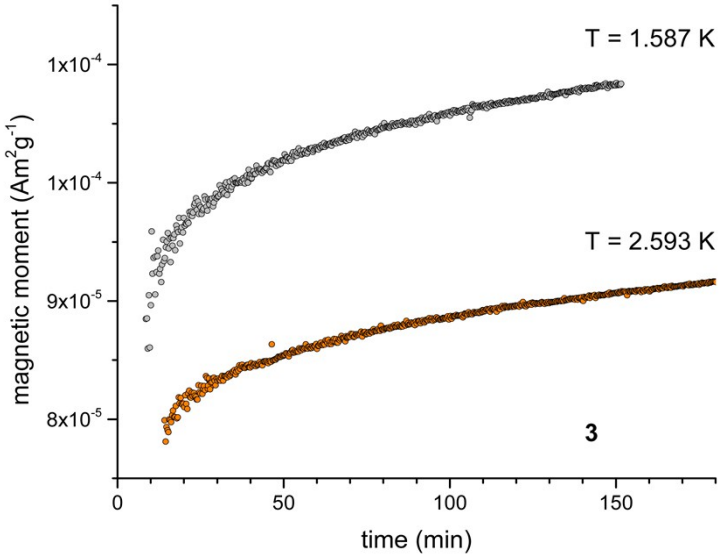

Figure S4. Magnetic moment vs. time plot for **3** recorded at 1.587 (grey) and 2.593 K (orange) in zero applied magnetic field after a 70 kOe field-cooling sequence.

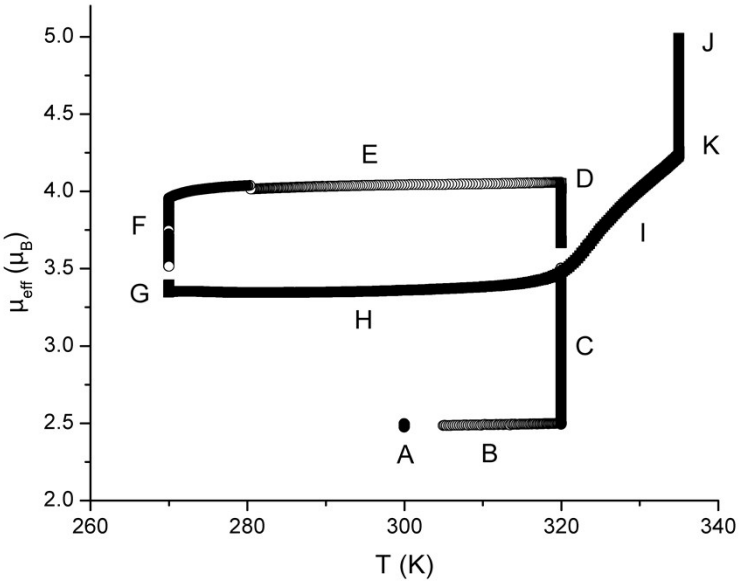

Figure S5. Effective magnetic moment (μ_{eff}) vs. T plot for complex **4. A:** starting point at 300 K; **B:** heating sequence to 320 K; **C:** isothermal N_2 release at 320 K; **D:** endpoint after *ca.* 23 h; **E:** cooling sequence to 270 K; **F:** isothermal N_2 binding; **G:** endpoint after approx. 14 h; **H+I:** heating sequence to 335 K; **I:** gradual N_2 release during the heating sequence; **K:** isothermal N_2 release at 335 K; **J:** endpoint after *ca.* 10 h (at 335 K).

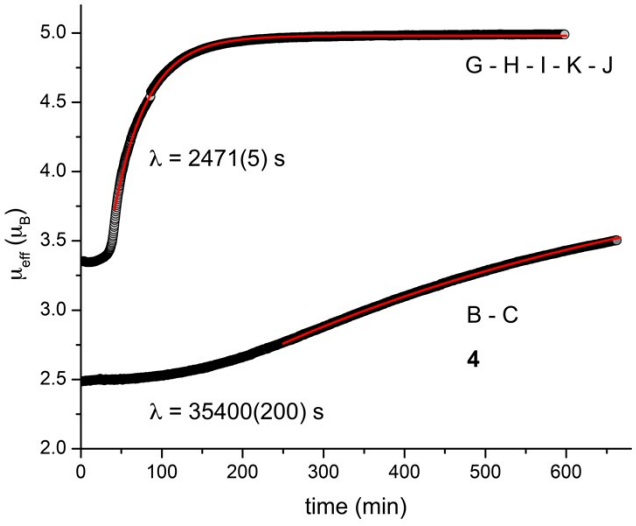

Figure S6. Effective magnetic moment (μ_{eff}) vs. time plot for isothermal N_2 release for complex **4** without a correction of the molar mass reduction of **4** after N_2 release. Symbols: experimental data, measured at T = 320 and 335 K, (B-C and G-H-I-K-J, respectively, cf. Figure S5); lines: fit on the basis of an exponential decay law, i.e. $\mu(t) = \mu(0) + \{\mu(\infty)-\mu(0)\}\ [1-\exp(-t/\lambda)]$.

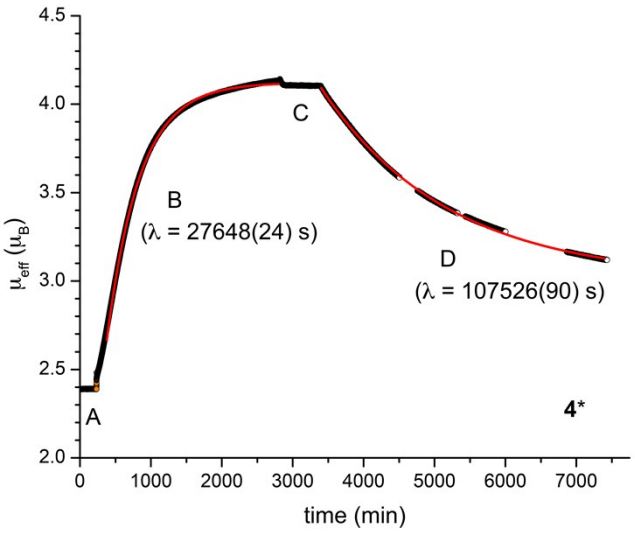

Figure S7. Effective magnetic moment (μ_{eff}) vs. time plot for isothermal N_2 release for complex **4** (measured with a new sample of **4**; denoted here as **4***) without a correction of the molar mass reduction of **4** after N_2 release. Symbols: experimental data, measured at T = 300 (A), 327.5 (B), 300 (C) and 280 K (D); lines: fit on the basis of an exponential decay law, i.e. $\mu(t) = \mu(0) + \{\mu(\infty)-\mu(0)\}\ [1-\exp(-t/\lambda)]$ and $\mu(t) = \mu(0) + \{\mu(0)-\mu(\infty)\}\ \exp(-(t-t_0)/\lambda)$, respectively.

5. Zero-field ^{57}Fe Mössbauer studies for 3 and 4

General considerations. Zero-field ^{57}Fe Mössbauer spectroscopy measurements were performed on a conventional transmission spectrometer with a Janis closed-cycle cryostat and sinusoidal velocity sweep. Polycrystalline powders of **3** and **4** were prepared with an area density corresponding to *ca.* 0.11–0.22 mg ^{57}Fe/cm^2 and were filled in sample containers made of Teflon or PEEK. After positioning the sample containers, the sample chamber was evacuated, flushed five times with helium gas and kept at ca. 10-80 mbar during the measurement. The temperature was measured with a calibrated Si diode located close to the sample container providing a temperature stability of better than 0.1 K. The activity of the Mössbauer source used was about 15 mCi of ^{57}Co in a rhodium matrix, which was stored at ambient temperatures during the measurement. Supplementary measurements on an identical prepared sample of complex **3** at temperatures below T = 20 K were performed on a spectrometer with a CryoVac continuous flow cryostat with comparable specifications, geometry and sample environments as described above. The activity of the Mössbauer source used was about 20 mCi of ^{57}Co in a rhodium matrix. The isomer shifts (δ) were specified relative to metallic iron at room temperature, but were not corrected in terms of second order Doppler shift.

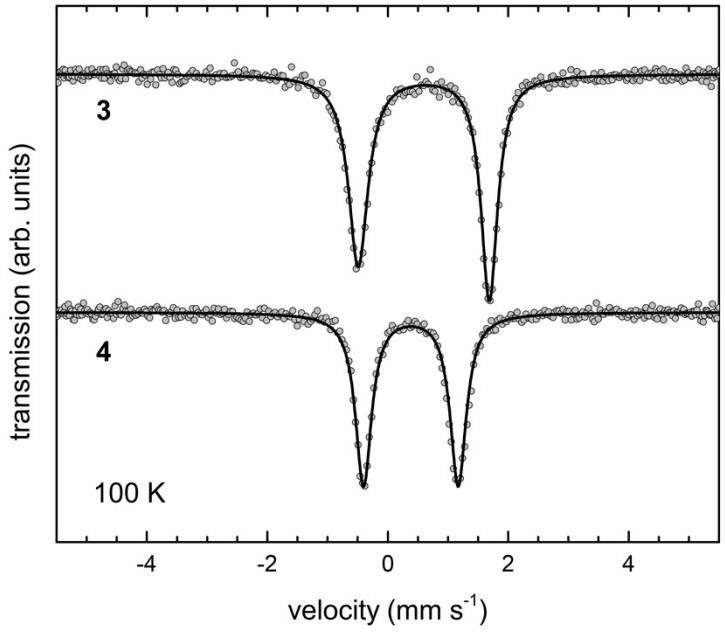

Figure S8. Zero-field Mössbauer spectra for **3** and **4** recorded at T = 100 K. Symbols: experimental data; lines: fit with Lorentzian lines (**4**) or on the basis of the Blume-Tjon relaxation model (**3**).[7]

Table S1. Mössbauer parameters for complex **3**. The analysis of the experimental data was performed by use of the stochastic Blume-Tjon relaxation model.[7] The isomer shifts (δ) were specified relative to metallic iron at room temperature, but were not corrected in terms of second order Doppler shift. The quadrupole splitting is given by $\Delta E_Q = 2\ \varepsilon$ with $\varepsilon = e^2\ q\ Q/4$ and $\eta = 0$ (with constants e, q, Q, η in their usual meaning).

T (K)	δ (mm s^{-1})	ε (mm s^{-1})	Γ_{HWHM} (mm s^{-1})	v_c (mm s^{-1})	H_{int} (kOe)
150	0.691(4)	-1.086(4)	0.159*	- [a]	244*
100	0.719(2)	-1.089(2)	0.159(5)	201(32)	244*
60	0.724(5)	-1.089(5)	0.198(8)	73(9)	244*
40	0.737(10)	-1.077(10)	0.235(10)	23(2)	244*
20 [b]	0.869(42) 0.869(41)	-1.030(30) -0.928(57)	0.3* 0.422(69)	19(5) 0.9(1)	244* 244(4)

[a] Fast dynamic relaxation limit; [b] site population: *ca.* 1:4; * fixed value.

Table S2. Mössbauer parameters for complex **4**. The isomer shifts (δ) were specified relative to metallic iron at room temperature, but were not corrected in terms of second order Doppler shift.

T (K)	δ (mm s^{-1})	ΔE_Q (mm s^{-1})	Γ_{HWHM} (mm s^{-1})
150	0.486(3)	1.543(5)	0.159(4)
100	0.505(3)	1.573(5)	0.163(4)
20	0.523(2)	1.594(4)	0.161(3)

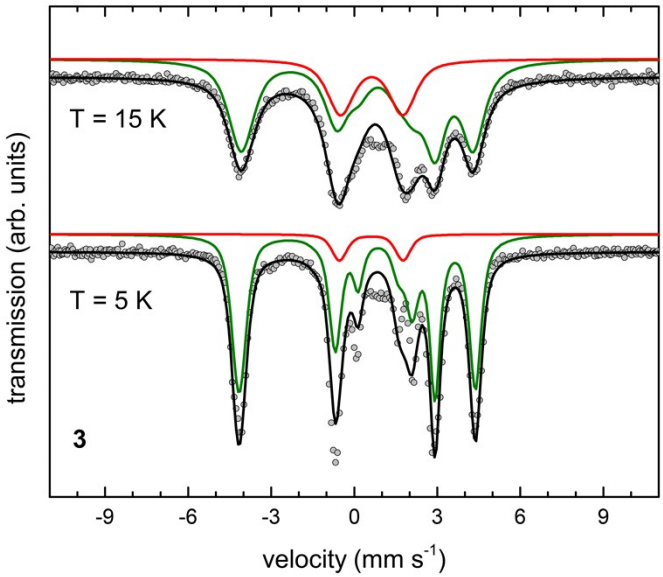

Figure S9. Supplementary zero-field Mössbauer spectra for **3** recorded at T = 15 and 5 K. Symbols: experimental data; lines: fit with a full static Hamiltonian approach.[8]

Table S3. Mössbauer parameters for complex **3**. The analysis of the experimental data was performed employing a full static Hamiltonian approach.[8] The isomer shifts (δ) were specified relative to metallic iron at ambient temperature, but they were not corrected for the second order Doppler shift. η and θ denote the asymmetry parameter and the angle between the local magnetic field at the ^{57}Fe nucleus site H_{int} and the V_{zz} component of the electric field gradient tensor, respectively. The angle between H_{int} and V_{xx} was fixed to ϕ = 0. To account for the relative intensities in the individual spectra shown in Figure S9, we also used a Gaussian distribution of the quadrupole splittings for the fit (given by a Gaussian line width of 0.10 and 0.33 mm s^{-1} at T = 15 and 5 K, respectively). The parameters δ, ΔE_Q, Γ_{HWHM}, η and θ were simultaneously fitted for the two non-equivalent Fe sites considered by this analysis.

T (K)	δ (mm s^{-1})	ΔE_Q (mm s^{-1})	Γ_{HWHM} (mm s^{-1})	H_{int} (kOe)	η	θ
15 [a]	0.773(3)	-2.263(10)	0.491(5)	231.1(4)	0.15(1)	25.1(2)

	0.773(3)	-2.263(10)	0.491(5)	0*	0.15(1)	25.1(2)
5 [b]	0.734(1) 0.734(1)	-2.292(4) -2.292(4)	0.202(3) 0.202(3)	233.9(1) 0*	0.15* 0.15*	27.0(1) 27.0(1)

[a] site population: *ca.* 3:1; [b] site population: *ca.* 9:1; * fixed value.

6. Solid-state X-band EPR spectra for 3 and 4

X-band EPR spectra were recorded on a Bruker EMX spectrometer with an OXFORD ESR900 continuous flow cryostat at T = 3.9 K. Polycrystalline powders of complexes **3** and **4**, respectively, were prepared in quartz tubes (707-SQ-250M, Wilmad-LabGlass). To provide a homogeneous spatial distribution of the sample we diluted them in dry boron nitride. The spectra were simulated with EasySpin 5.1.8[9] yielding a fair agreement with the experimental data for compounds **3** and **4** (Figures S10 and S11). One complication in the simulation stems from the fact that for both compounds, the presence of an impurity phase was visible in the measured EPR spectra, i.e. an *S*=1/2 impurity (presumably complex **4**) in case of complex **3** and an *S*=3/2 impurity (presumably complex **3**) in case of complex **4**. For complex **4**, we also considered a coupling of the electronic magnetic moment with the two individual nuclear magnetic moments of the two nitrogen atoms of the N_2 ligand coordinated to the iron atom. The influence of the two nitrogen atoms within the NHC ligand appears to be negligible in both complexes **3** and **4**.

Table S4. EPR parameters for complexes **3** and **4** based on a simulation presented in Figures S9 and S10. $HStrain_n$ describes the line broadening caused by unresolved hyperfine couplings, $gStrain_n$ denotes the g strain for the electron spin, lwpp denotes the peak-to-peak line width for isotropic broadening and $^{14N}A_n$ denotes the hyperfine couplings with the two individual nitrogen atoms (*I*=1) for the N_2 ligand in compound **4**.

	3		**4**	
	product	impurity	product	impurity
S	3/2	1/2	1/2	3/2
g_1	4.35384	2.33690	2.2124	4.2835
g_2	1.97971	1.97825	2.0468	2.1251
g_3	1.94315	2.10408	2.1206	1.9325
$HStrain_1$ / MHz	1	-	1.5486	-
$HStrain_2$ / MHz	1	-	1.1607	-
$HStrain_3$ / MHz	1	-	0.1517	-

$gStrain_1$	0.1040620	-	0.03341	-
$gStrain_2$	0.0879485	-	0.07350	-
$gStrain_3$	0.0948024	-	0.02254	-
lwpp /mT	-	4	-	3
weight	0.301737	0.786363	6	0.3
$^{14N}A_1$, $^{14N}A_2$ /mT	-	-	5.25, 10.52	-

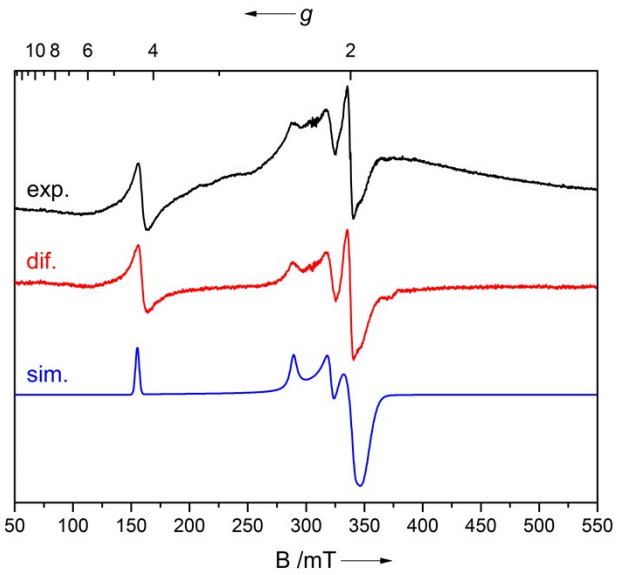

Figure S10. X-band EPR spectrum for **3** recorded at T = 3.9 K with ν = 9.464365 GHz and a modulation amplitude of 8 G. Lines: experimental data (black); difference spectrum (red) after subtraction of the cavity background signal; simulation (blue) with an *S*=3/2 main signal and an *S*=1/2 impurity signal. The parameters of the simulation are summarised in Table S4.

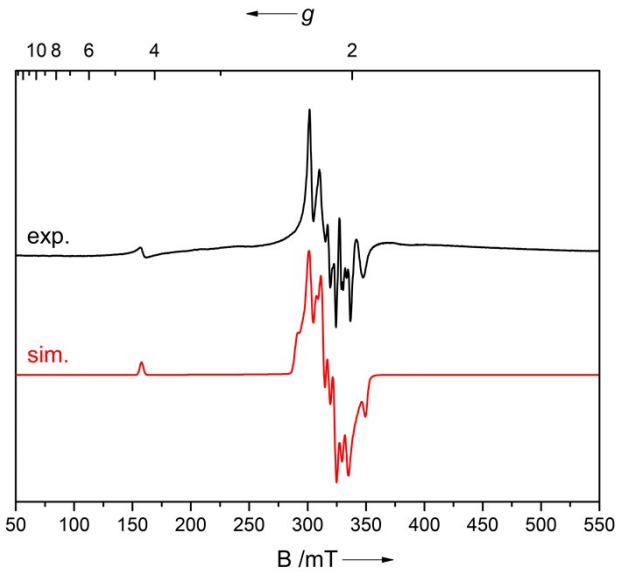

Figure S11. X-band EPR spectrum for **4** recorded at T = 3.9 K with ν = 9.464325 GHz and a modulation amplitude of 8 G. Lines: experimental data (black); simulation (red) with an *S*=1/2 main signal and an *S*=3/2 impurity signal. The parameters of the simulation are summarised in Table S4.

7. Computational details

All calculations were carried out with the program Gaussian 09[10] and the B3LYP functional (with and without empirical dispersion correction (D3)) as incorporated in Gaussian 09.[10] No symmetry restrictions were imposed (C_1). C, H, N and Fe were represented by an all-electron 6-311G(d,p) basis set. The nature of the extrema (minima) was established with order analytical frequency calculations. The zero-point vibration energy (ZPE) and entropic contributions were estimated within the harmonic potential approximation. The Gibbs free energy, ΔG, was calculated for T= 298.15 K and 1 atm. Geometrical parameters were reported within an accuracy of 10^{-3} Å and 10^{-1} degrees. Inclusion of dispersion effects result in a small contraction of the intramolecular bond distances, while the overall thermodynamics are not changed significantly.

Table S5. Energies of the optimized structures

Compound	spin-state	DFT functional	E(0 K)[a] [Ha]	H(298 K)[b] [Ha]	G(298 K)[b] [Ha]
[Cp'Fe(I*i*Pr$_2$Me$_2$)] (**3**)	*S* = 1/2	B3LYP	-2469.257559	-2469.218827	-2469.324078
		B3LYP+D3	-2469.371303	-2469.333302	-2469.436656
	S = 3/2	B3LYP	-2469.291972	-2469.252159	-2469.361289
		B3LYP+D3	-2469.408628	-2469.369845	-2469.475874

[Cp'Fe(I*i*Pr$_2$Me$_2$)(η^1-N$_2$)] (**4**)	*S* = 1/2	B3LYP	-2578.846518	-2578.804875	-2578.917029
		B3LYP+D3	-2578.970539	-2578.929734	-2579.039204
	S = 3/2	B3LYP	-2578.842387	-2578.799250	-2578.917271
		B3LYP+D3	-2578.967584	-2578.925524	-2579.039482
N_2	*S* = 0	B3LYP	-109.550354	-109.54705	-109.568787
		B3LYP+D3	-109.568787	-109.568787	-109.568787

[a]DFT energy incl. ZPE. [b]standard conditions: *T* = 298.15 K and *p* = 1 atm.

Table S6. Comparison between experimental and computed structures for [Cp'Fe(I*i*Pr$_2$Me$_2$)] (**3**)

Bond distances (Å) and angles (°)	X-ray data	S=1/2 (B3LYP)	S=1/2 (B3LYP+D3)	S=3/2 (B3LYP)	S=3/2 (B3LYP+D3)
Fe-C(Cp') (ave)	2.2170±0.0526	2.142±0.039	2.126±0.035	2.272±0.092	2.247±0.096
Fe-Cp'$_{cent}$	1.85	1.76	1.74	1.919	1.89
Fe-Cp'$_{plane}$	1.85	1.76	1.74	1.91	1.88
Fe-C18	2.009(3)	1.970	1.950	2.021	1.998
Cp'$_{cent}$- Fe-C18	163.67	144.8	143.9	154.0	148.7

Table S7. Comparison between experimental and computed structures for [Cp'Fe(I*i*Pr$_2$Me$_2$)(η^1-N$_2$)] (**4**)

Bond distances (Å) and angles (°)	X-ray data	S=1/2 (B3LYP)	S=1/2 (B3LYP+D3)	S=3/2 (B3LYP)	S=3/2 (B3LYP+D3)
Fe-C(Cp') (ave)	2.1342±0.0264	2.176±0.049	2.157±0.049	2.368±0.0944	2.340±0.0725
Fe-Cp'$_{cent}$	1.75	1.80	1.78	2.03	2.00
Fe-Cp'$_{plane}$	1.75	1.80	1.78	2.02	1.99
Fe-N3	1.7623(11)	1.776	1.774	1.907	1.900
Fe-C18	1.9688(12)	1.998	1.973	2.126	2.091
Cp'$_{cent}$- Fe-N3	136.46	127.6	128.5	119.6	120.7
Cp'$_{cent}$- Fe-C18	131.15	137.4	135.1	143.3	138.5
C18-Fe-N3	90.46(5)	92.7	93.7	97.0	100.7
N3-N4	1.1311(16)	1.125	1.125	1.19	1.12

Table S8. Thermodynamics of N_2 binding to [Cp'Fe(I*i*Pr$_2$Me$_2$)] (**3**) considering different spin state alternatives

Reaction	DFT functional	ΔE(0 K)[a] [kcal mol^{-1}]	ΔH(298 K)[b] [kcal mol^{-1}]	ΔG(298 K)[b] [kcal mol^{-1}]
3 (*S*=1/2) + N_2 (*S*=0) → **4** (*S*=1/2)	B3LYP	-24.22	-24.47	-15.16
	B3LYP+D3	-30.67	-30.99	-21.19
3 (*S*=1/2) + N_2 (*S*=0) → **4** (*S*=3/2)	B3LYP	-21.63	-20.94	-15.31
	B3LYP+D3	-28.82	-28.35	-15.31
3 (*S*=3/2) → **3** (*S*=1/2)	B3LYP	21.59	20.92	23.35
	B3LYP+D3	23.42	22.93	24.61
3 (*S*=3/2) + N_2 (*S*=0) → **4** (*S*=3/2)	B3LYP	-0.04	-0.03	8.04
	B3LYP+D3	-5.40	-5.41	3.25
3 (*S*=3/2) + N_2 (*S*=0) → **4** (*S*=1/2)	B3LYP	-2.63	-3.56	8.19
	B3LYP+D3	-7.25	-8.06	3,42
4 (*S*=3/2)→ **4** (*S*=1/2)	B3LYP	-2.59	-3.53	0.15
	B3LYP+D3	-1.89	-2.64	0.17

[a]DFT energy incl. ZPE. [b]standard conditions: *T* = 298.15 K and *p* = 1 atm.

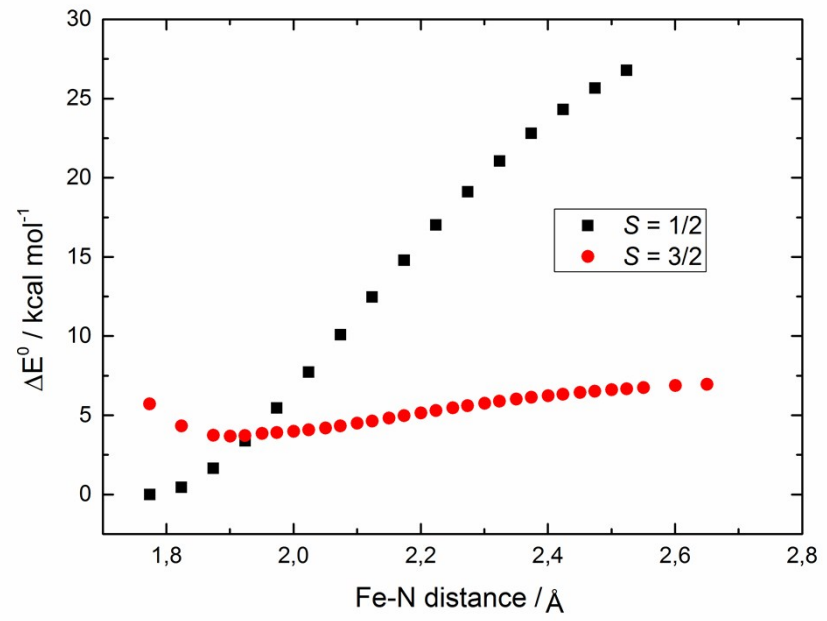

Figure S12. Potential energy surface (PES) scan (B3LYP/6-311 G(d,p)) along the Fe-N bond distance in [Cp'Fe(I*i*Pr$_2$Me$_2$)(η^1-N$_2$)] (**4**) assuming an *S* = 1/2 or *S* = 3/2 electronic ground state. PES crossing occurs at a Fe-N distance of *ca.* 1.92 Å and with a barrier ΔE^0 of *ca.* 3.6 kcal mol^{-1} (above the electronic ground state *S* = 1/2 of **4**.

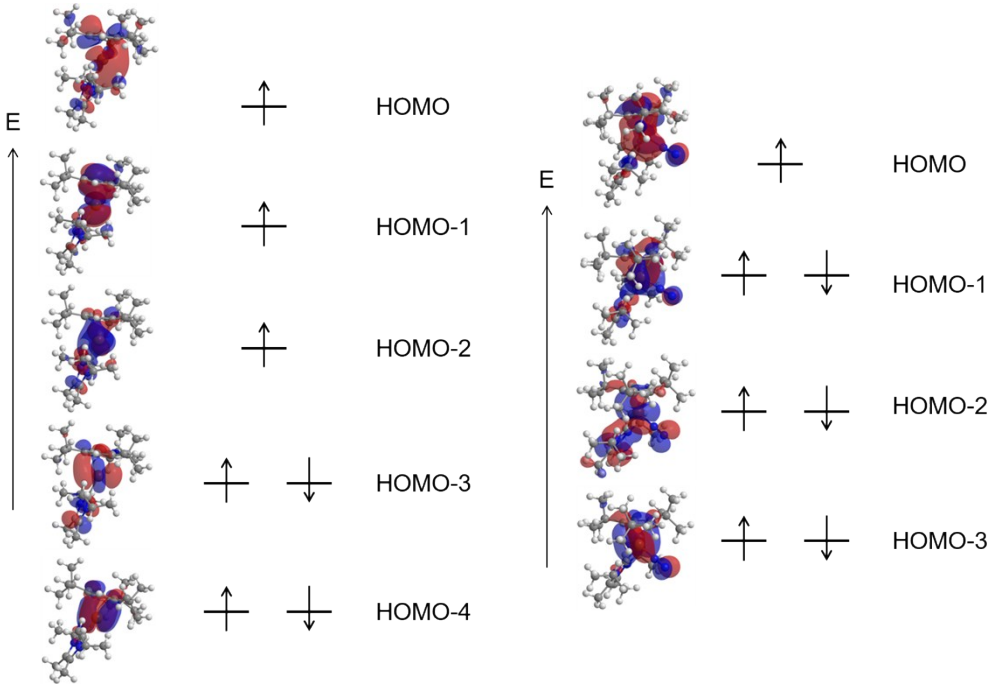

Figure S13. (Biorthogonalized) Kohn Sham orbitals (B3LYP/6-311 G(d,p)) for complexes **3** (left) and **4** (right).

8. References

1. M. Reiners, D. Baabe, K. Harms, M. Maekawa, C. G. Daniliuc, M. Freytag, P. G. Jones and M. D. Walter, *Inorg. Chem. Front.*, 2016, **3**, 250-262.
2. M. A. Schwindt, T. Lejon and L. S. Hegedus, *Organometallics*, 1990, **9**, 2814-2819.
3. G. M. Sheldrick, *SHELXL-97, Program for the Refinement of Crystal Structure from Diffraction Data*, (1997), University of Göttingen, Göttingen, Germany.
4. G. M. Sheldrick, *Acta Cryst.*, 2008, **A64**, 112-122.
5. M. D. Walter, M. Schultz and R. A. Andersen, *New J. Chem.*, 2006, **30**, 238-246.
6. G. A. Bain and J. F. Berry, *J. Chem. Educ.*, 2008, **85**, 532-536.
7. M. Blume and J. A. Tjon, *Phys. Rev.*, 1968, **165**, 446-456.
8. R. A. Brand, *WinNormos-for-Igor*, Version 3.0 (May 2009).
9. S. Stoll and A. Schweiger, *J. Magn. Reson.*, 2006, **178**, 42-55.
10. M. J. Frisch, G. W. Trucks, H. B. Schlegel, G. E. Scuseria, M. A. Robb, J. R. Cheeseman, G. Scalmani, V. Barone, B. Mennucci, G. A. Petersson, H. Nakatsuji, M. Caricato, X. Li, H. P. Hratchian, A. F. Izmaylov, J. Bloino, G. Zheng, J. L. Sonnenberg, M. Hada, M. Ehara, K. Toyota, R. Fukuda, J. Hasegawa, M. Ishida, T. Nakajima, Y. Honda, O. Kitao, H. Nakai, T. Vreven, J. A. J. Montgomery, J. E. Peralta, F. Ogliaro, M. Bearpark, J. J. Heyd, E. Brothers, K. N. Kudin, V. N. Staroverov, R. Kobayashi, J. Normand, E. Raghavachari, A. Rendell, J. C. Burant, S. S. Iyengar, J. Tomasi, M.

Cossi, N. Rega, J. M. Millam, M. Klene, J. E. Knox, J. B. Cross, V. Bakken, C. Adamo, J. Jaramillo, R. Gomperts, R. E. Stratmann, O. Yazyev, A. J. Austin, R. Cammi, C. Pomelli, J. W. Ochterski, R. L. Martin, K. Morokuma, V. G. Zakrzewski, G. A. Voth, P. Salvador, J. J. Dannenberg, S. Dapprich, A. D. Daniels, O. Farkas, J. B. Foresman, J. V. Ortiz, J. Cioslowski and D. J. Fox, (2009) Gaussian, Inc., Wallington CT.